ARTICLES SCIENCE CHINA Materials

mater.scichina.com link.springer.com

Published online 13 October 2017 | https://doi.org/10.1007/s40843-017-9122-4

Sci China Mater 2018, 61(1): 48–56

Urchin-like FeOOH hollow microspheres decorated with MnO_2 for enhanced supercapacitor performance

Kun Du[1,2], Guijuan Wei[1,2], Fuzhen Zhao[1,2], Chao An[2], Hui Wang[1], Jinquan Li[1,2] and Changhua An[1,2*]

ABSTRACT **Ultrathin MnO_2 decorated hierarchical urchin-like FeOOH hollow micro-nanospheres have been designed and synthesized through a facile hydrothermal route. The microspheres are made of FeOOH nanofibers with a diameter of 10 nm. Due to the synergetic effect between the unique FeOOH hollow micro/nanostructures and ultrathin MnO_2 layer, the as-fabricated FeOOH@MnO_2 hybrid electrode exhibits a high specific capacitance of 1192 F g^{-1} at a current density of 1 A g^{-1}. It also reveals high rate capabilities and superior stability. Moreover, the asymmetric supercapacitor (ASC) assembled from the FeOOH@MnO_2 and the active carbon (AC) delivers a high energy density of 40.2 W h kg^{-1} at a power density of 0.78 kW kg^{-1}, and the energy density could remain 10.4 W h kg^{-1} under a condition of high power density of 11.7 kW kg^{-1}.**

Keywords: FeOOH, MnO_2, hollow structures, supercapacitor

INTRODUCTION

With the ever-increasing environmental issues and the continuous demand for energy consumption, great efforts have been made to develop sustainable and environmentally friendly alternative energy sources and energy storage devices [1–5]. Supercapacitors known as electrochemical capacitors (ECs) have triggered significant researches for their potential applications in portable electronics, electric or hybrid electric vehicles, owing to their large power density, fast recharge ability, long cycling life, low maintenance cost and high reliability [6–9]. The performance of ECs is mainly dependent on the electrode materials. Most EC electrode materials are categorized into three main groups: carbonaceous materials [10,11], transitional metal oxides/hydroxides [12,13], and conducting polymers [14]. Among them, transition-metal-based oxides or hydroxides have received much attention due to their higher specific capacitances [15–19].

Iron oxides/hydroxides including Fe_2O_3, Fe_3O_4, and FeOOH exhibit great promise as anode materials [20–25], owing to their high theoretical capacitance, low cost, and environmental benignity. However, relatively low electrical conductivity and stability limit their capacitances at high current densities. One promising approach to improve their performance is to combine other metal oxides in a composite. Manganese dioxide (MnO_2) with favorable properties and high theoretical specific capacitance (1370 F g^{-1}) makes it a promising electrode material in energy storage and conversion devices [26–30]. Furthermore, three-dimensional (3D) transitional metal oxides/hydroxides nanostructures assembled from low-dimensional building blocks [31–34] exhibit enhanced properties compared to their bulk counterparts by offering a large specific surface area, high surface/body ratios, the enhanced permeability for the electrolyte ions, and rich electrochemically active sites [35]. Therefore, the construction of 3D FeOOH@MnO_2 is a rational way to realize a high performance EC.

In this work, we have developed a facile strategy for the design and fabrication of novel 3D hierarchical FeOOH@MnO_2 hollow microspheres. The as-prepared FeOOH@MnO_2 produced a higher specific capacitance (1192 F g^{-1} at 1 A g^{-1}) and better cycling performance than pristine FeOOH, owing to the synergetic effects between the hierarchical FeOOH hollow microspheres and ultrathin MnO_2 layer. Moreover, the asymmetric supercapacitor (ASC) device assembled from the FeOOH@MnO_2 and active carbon (AC) delivers a high energy density of 40.2 W h kg^{-1} at a power density of 0.78 kW kg^{-1}, and the

[1] Tianjin Key Laboratory of Organic Solar Cells and Photochemical Conversion, College of Chemistry and Chemical Engineering, Tianjin University of Technology, Tianjin 300384, China

[2] State Key Laboratory of Heavy Oil Processing, College of Science and College of Chemical Engineering, China University of Petroleum, Qingdao 266580, China

* Corresponding author (email: anch@tjut.edu.cn)

energy density could remain 10.4 W h kg^{-1} under a high power density of 11.7 kW kg^{-1}.

EXPERIMENTAL SECTION

Materials

The $FeSO_4·7H_2O$, $KMnO_4$ and glycerol (Sinopharm Chemical Reagent Co. Ltd (China)) were analytical grade and used without further purification.

Preparation of FeOOH@MnO_2

In a typical procedure, 0.111 g $FeSO_4·7H_2O$ was dissolved in a mixture of 35 mL of deionized water and 5 mL glycerol. After stirring for several minutes, the mixture was transferred into a 50-mL Teflon-lined stainless steel autoclave and heated at 120°C for 24 h. After being cooled down to room temperature naturally, the products were collected by centrifugation and washed with deionized water and ethanol. The as-obtained FeOOH was then dispersed into 10 mL of 0.02 mol L^{-1} $KMnO_4$ solution and stirred at room temperature for 30 min. The resulting product was harvested following a similar procedure, and dried at 60°C for 12 h.

Characterization

The surface morphology and size of the as-prepared samples were analyzed by field emission scanning electronic microscopy (FE-SEM, Hitachi S-4800) and transmission electronic microscopy (TEM, JEM-2100F), equipped with energy dispersive X-ray spectroscopy (EDS). The crystalline phases of the samples were analyzed by X-ray powder diffraction (XRD) (PANalytical B. V., Almelo, The Netherlands) on a Philips X'Pert diffractometer with Cu Kα irradiation (λ = 0.15418 nm). The Brunauer-Emmett-Teller (BET) surface areas were analyzed by nitrogen adsorption with Micromeritics ASAP 2020 nitrogen adsorption apparatus. The sample was degassed at 100°C prior to N_2 adsorption. The chemical composition was investigated by X-ray photoelectronic spectroscopy (XPS), performed on an Axis Ultra, Kratos (UK) at monochromatic Al K radiation (150 W, 15 kV, and 1486.6 eV).

Electrochemical measurements

The electrodes were prepared by mixing 80 wt.% of the sample, 15 wt.% of the acetylene black and 5 wt.% of the polytetrafluoroethylene (PTFE) in ethanol, and then the paste was pressed onto nickel foams. Electrochemical tests were performed on an electrochemical workstation (CHI 760E, Shanghai Chenhua Co. Ltd., China) with a three-electrode configuration in 2 mol L^{-1} KOH electrolyte at room temperature. The FeOOH@MnO_2 hollow spheres were used as the working electrodes, platinum foil as the counter electrode and standard Hg/HgO as the reference electrode, respectively. Cyclic voltammetry (CV) was performed between 0.1 and 0.7 V at scan rates of 5, 10, 15, 20, 30, 50, and 100 mV s^{-1} and galvanostatic charge-discharge (GCD) was tested between 0 and 0.53 V at current densities of 1, 2, 3, 5, 10, and 20 A g^{-1}, respectively. Moreover, electrochemical impedance spectroscopy (EIS) tests were conducted with frequencies ranging from 0.01 to 100,000 Hz. The specific capacitance values (C_{sc}) were calculated from the GCD curves according to the following equation:

$$C_{sc} = I\Delta t / \Delta V m, \quad (1)$$

where I (A) is the current, Δt (s) is the discharge time, ΔV (V) is the voltage window, and m (g) is the mass of active component, respectively.

The ASC was assembled with AC as the negative electrode and the FeOOH@MnO_2 as the positive electrode. For an ASC, the charge stored in one electrode depends on the following formula:

$$q = C \times \Delta V \times m. \quad (2)$$

According to the charge balance ($q^+ = q^-$), the mass balance between the positive and negative electrodes can be derived:

$$m^- / m^+ = (C^+ \times \Delta V^+) / (C^- \times \Delta V^-), \quad (3)$$

where C^+ and C^- (F g^{-1}) are specific capacitance of the single electrode, ΔV^+ and ΔV^- (V) are the corresponding working potential range, and m^+ and m^- (g) are the mass of the respective electrodes. The energy density (E) and power density (P) are two key parameters for evaluating practical performance of the supercapacitor, which can be obtained from the following equations:

$$E = 0.5CV^2, \quad (4)$$

$$P = E / t, \quad (5)$$

where C (F g^{-1}) is the capacitance of ASCs, V (V) is the cell voltage, and t (s) is the discharge time, respectively.

RESULTS AND DISCUSSION

As shown in Fig. 1a, the FeOOH display hierarchical urchin-like microspheres with an even diameter of 1 μm. The high-magnification SEM image (Fig. 1b) shows the microspheres are assembled from numerous nanofibers with an average diameter of 10 nm, which have densely and firmly covered the surface of microspheres in radiative mode. After being coated with MnO_2, the FeOOH@MnO_2 (Fig. 1c, d) retains original shape. As

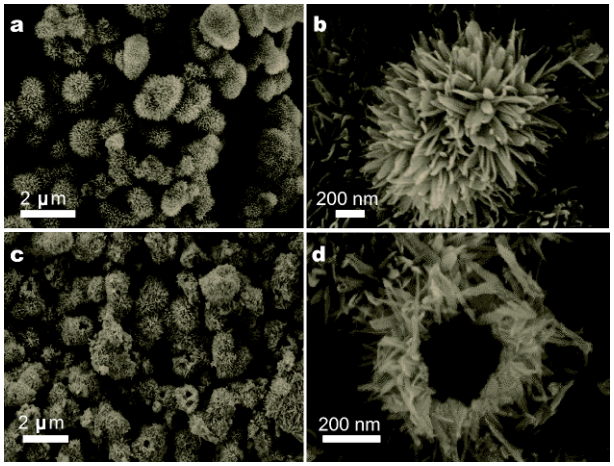

Figure 1 SEM images of FeOOH (a, b) and FeOOH@MnO_2 (c, d).

seen from the marked broken spheres, these microspheres display a hollow structure, and a large void can be clearly discerned.

Fig. 2a shows the XRD patterns of the FeOOH and the FeOOH@MnO_2 products. All the diffraction peaks are assigned unambiguously to the orthorhombic-phase of FeOOH (JCPDF Card No. 29-713). No peaks from impurities are detected. The diffraction patterns of MnO_2 are absent owing to its low content and crystallinity. TEM image of FeOOH (Fig. 2b) shows hollow microspheres with the inner diameter about 500 nm. After decorating with MnO_2, the surfaces become rough (Fig. 2c). As shown in Fig. 2d, the HRTEM image displays lattice fringes of 0.219 nm and 0.236 nm , which are in accord with the (220) plane of α-FeOOH and the (111) plane of ramsdellite MnO_2, respectively, indicating the MnO_2 layer has been formed on the surfaces of α-FeOOH. EDS mappings, shown in Fig. 2f–h, of several FeOOH@MnO_2 nanofibers (Fig. 2e) confirm the presence of elements of Fe, O and Mn in the FeOOH@MnO_2 hierarchical microspheres. The TEM- EDS spectrum (Fig. 2i) shows the presence of Fe, O and Mn characteristic peaks, consistent with the mapping result. The atomic percentages of Fe and Mn are 1.6% and 31.4%, respectively, indicating the ratio of MnO_2/FeOOH is 0.051.

The chemical composition and the valence state of the elements of FeOOH@MnO_2 have been further confirmed by XPS analysis (Fig. 3). The survey spectrum shows the Fe, O and Mn are present in the hybrid (Fig. 3a). The Fe 2p spectrum exhibits two main peaks at 711.1 and 724.8 eV in addition to their shake-up satellite peaks at 719.1 and 732.4 eV (Fig. 3b) [36–38]. The O 1s spectrum can be fitted into two peaks, where the lower binding energy peak at 529.9 eV is associated with an Fe–O–Fe bond, whereas the higher peak at 531.4 eV is due to an Fe–O–H bond (Fig. 3c) [36,38,39]. As shown in Fig. 3d, the binding energies of Mn $2p_{3/2}$ and Mn $2p_{1/2}$ located at 642.3 and 653.7 eV are assigned to Mn (IV) ions [40].

Fig. S1 reveals that the as-prepared materials exhibit type IV isotherm curves with a hysteresis loop in the range of 0.5–1.0 P/P_0, which is the characteristic of mesoporous material [41–43]. The surface area of FeOOH and FeOOH@MnO_2 was estimated to be 124.1 and 116.5 $m^2\ g^{-1}$, respectively, indicating that the surface area decreases slightly after coating MnO_2 on the surface of FeOOH. On the other hand, the total pore size distributions of the samples indicate that both samples have a narrow aperture distribution.

The electrochemical properties of the as-synthesized specimens were tested through CV, GCD, and EIS with a typical three-electrode configuration in a 2 mol L^{-1} KOH alkaline electrolyte. Fig. 4a compares the CV curves of the FeOOH@MnO_2 with FeOOH at a scan rate of 50 mV s^{-1} within a potential window ranging from 0.1 to 0.7 V (*vs.* Hg/HgO). The integral area for the CV curve of FeOOH@MnO_2 electrode is much larger than that of the FeOOH electrode, suggesting a significant improvement of capacitance. The comparison of GCD curves at a current density of 2 A g^{-1} further demonstrates the result (Fig. 4b). With MnO_2 cover, the discharging time is much higher than that for bare FeOOH.

In order to get more insights into the performance of the FeOOH@MnO_2 and the FeOOH electrodes, the CV tests were measured at various scan rates and the GCD were carried out at different current densities, respectively (Fig. 4c, d, and Fig. S2). As shown in Fig. 4c, a pair of redox peaks can be clearly observed, corresponding to the pseudocapacitive mechanism, which results from the reversible conversion between Fe^{3+} and Fe^{2+} ions [44]. The phase transformation reaction can be described as follows [45]:

$$FeOOH + H_2O + e^- \leftrightarrow Fe(OH)_2 + OH^-$$

In addition, the positions of anodic and cathodic peaks shift towards more anodic and cathodic direction at high scan rates, and the current density of the curves increases, which reveals the fast ionic and electronic transfer over the electrode surface. From the GCD curves (Fig. 4d), it can be seen that the plots are quasi-symmetrical, indicating that the as-prepared samples have an excellent reversible redox process. The specific capacitance of FeOOH@MnO_2 electrode reaches 1192, 1087, 911, 790, 660 and 560 F g^{-1} at current densities of 1, 2, 3, 5, 10 and

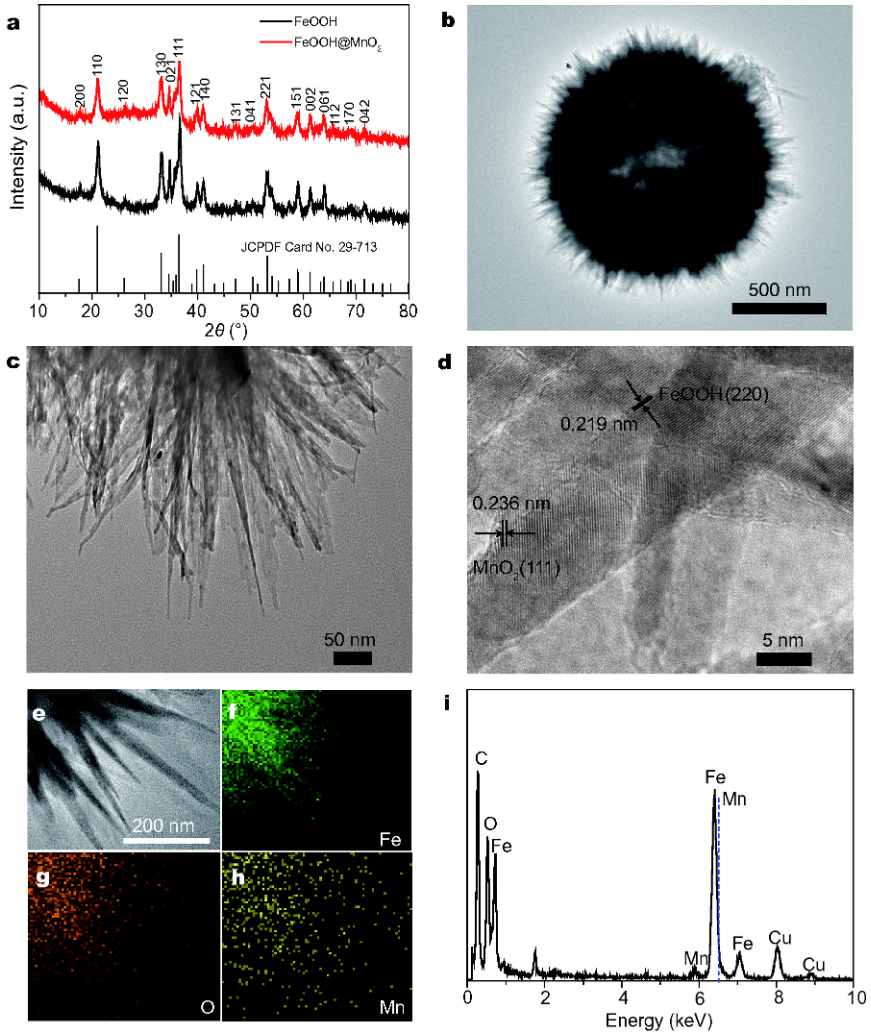

Figure 2 (a) XRD patterns of FeOOH and FeOOH@MnO_2; (b) TEM image of a FeOOH microsphere; (c) low-magnification and (d) high-resolution TEM image of FeOOH@MnO_2; (e–h) EDS elemental mapping from several hybrid nanofibers, and (i) EDS spectrum of the FeOOH@MnO_2 nanofibers shown in (e).

20 A g^{-1}, respectively, which are higher than bare FeOOH electrode (Fig. 4e) and reported data for MnO_2 (300 F g^{-1}) [46]. Remarkably, the FeOOH@MnO_2 electrode exhibits evident improvement in terms of capacity and rate performance. The FeOOH@MnO_2 electrode can maintain the capacitance retention of 95.1% after 1000 cycles at a high current density of 5 A g^{-1}, demonstrating its good stability in comparison with FeOOH electrode (89%) (Fig. 4f).

The EIS tests are used to understand the electrochemical reaction kinetics. The Nyquist plots of the two samples obtained in the frequency range of 100 kHz to 0.01 Hz are shown in Fig. S3. In the high-frequency region, the intercept of *X* axis for FeOOH@MnO_2 is smaller than that for FeOOH, showing its less bulk resistance. Similarly, the radius of the semicircle of FeOOH@MnO_2 is also less than that of FeOOH, meaning that the charge transfer over FeOOH@MnO_2 is faster. In the low-frequency region, the FeOOH@MnO_2 reveals a more vertical line, showing its better ion diffusion capacitance.

To further investigate the practical application of the FeOOH@MnO_2, the ASC was assembled with FeOOH@MnO_2 as the positive electrode and AC as the negative electrode (denoted as FeOOH@MnO_2//AC). The tests were performed in 2 mol L^{-1} KOH aqueous electrolyte with a voltage of 1.6 V. The electrochemical performance of the AC was firstly measured with the voltage range of −1.0 to 0.1 V (*vs.* Hg/HgO) (Fig. S4). The rec-

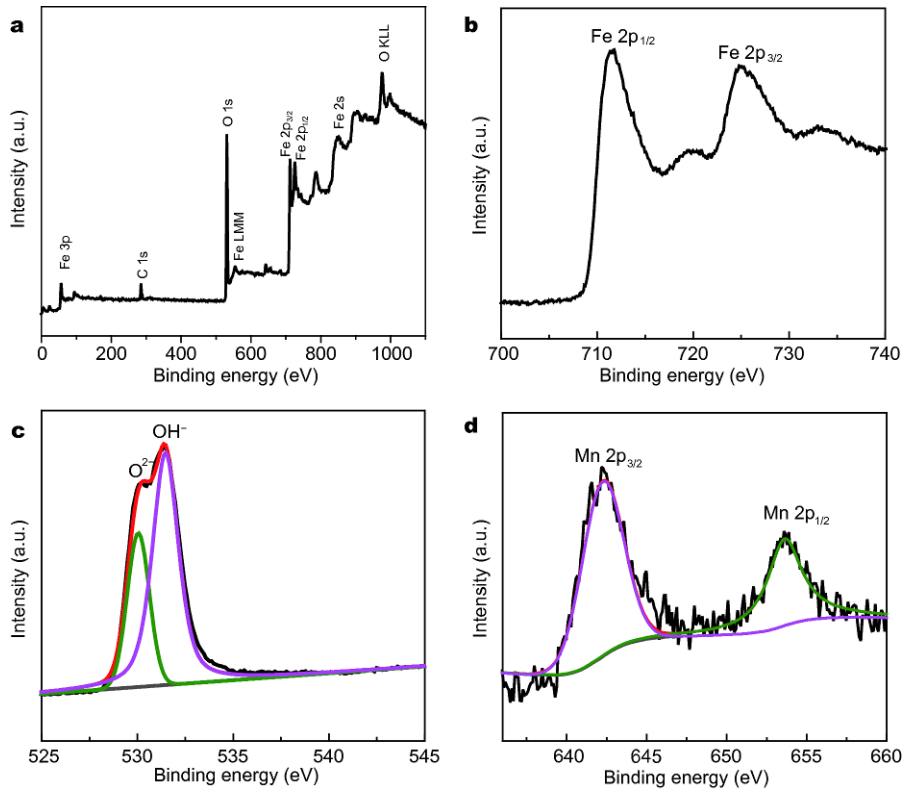

Figure 3 (a) XPS spectrum of α-FeOOH@MnO_2 and high-resolution XPS spectra of (b) Fe 2p, (c) O 1s, and (d) Mn 2p.

tangle-like CV curves in Fig. S4a show ideal double electric layer capacitor behavior. Before assembling, the CV comparison of both AC and FeOOH@MnO_2 electrodes were obtained at a scan rate of 30 mV s^{-1} in a three-electrode system (Fig. S4c). The specific capacitance of AC electrode has been estimated to be 90.9 F g^{-1} at a scan rate of 30 mV s^{-1}. According to the charge balance between the positive and negative electrodes, the mass balance can be obtained by Equation (3). As shown in Fig. S4d, the FeOOH@MnO_2//AC ASC was analyzed in different voltage windows at a scan rate of 50 mV s^{-1}, confirming that 1.6 V is a suitable voltage window.

Fig. 5a gives CV profiles of the ASC with scan rates ranging from 5 to 100 mV s^{-1}. A couple of redox peaks can be observed, resulting from the redox reaction in the FeOOH@MnO_2 electrode. In addition, the shape of the profiles is well maintained with increasing the scan rates, revealing a rapid charge-discharge characteristic of the device. Fig. 5b illustrates the GCD plots of the ASC tested at various current densities within a potential window from 0 to 1.56 V. The charge-discharge curves are all almost symmetric, exhibiting a rapid *I-V* response and desirable reversibility. The device has 119, 106.2, 101.4, 96, 77.6, 42.3 and 30.7 F g^{-1} at 1, 2, 2.5, 3, 5, 10 and 20 A g^{-1}, respectively, according to the GCD curves in Fig. 5c. The coulombic efficiencies of the ASC are 79.5%, 83.5%, 89.7%, 90.5%, 90.2%, 90.4% and 94.1% at a current densities from 1 A g^{-1} to 20 A g^{-1}, indicating that the effective transport of electrons promotes the Faradaic redox reaction on the electrode/electrolyte surface. The relationship between the power densities (*P*) and energy densities (*E*) was depicted in Ragone plot, which was further used to estimate the performance of the as-assembled ASC (Fig. 5c). A maximum energy density of 40.2 W h kg^{-1} was realized at a power density of 0.78 kW kg^{-1}, and the energy density could remain at 10.4 W h kg^{-1} under a high power density of 11.7 kW kg^{-1}. Moreover, the long-term stability test of the ASC was performed between 0 and 1.56 V at a constant current density of 5 A g^{-1}. As shown in the Fig. 5d, the specific capacitances of the ASC maintain 91% after 1000 cycles, showing its good stability. The enhanced electrochemical performance can be attributed to the unique 3D hollow shape wherein: (1) MnO_2 with high redox activity combining ordered FeOOH nanofibers would be helpful to increase the value of the specific capacitance [47]. The ultrathin MnO_2 layer is beneficial for the enhanced cyclic stability of FeOOH@MnO_2; (2) the effective contact area

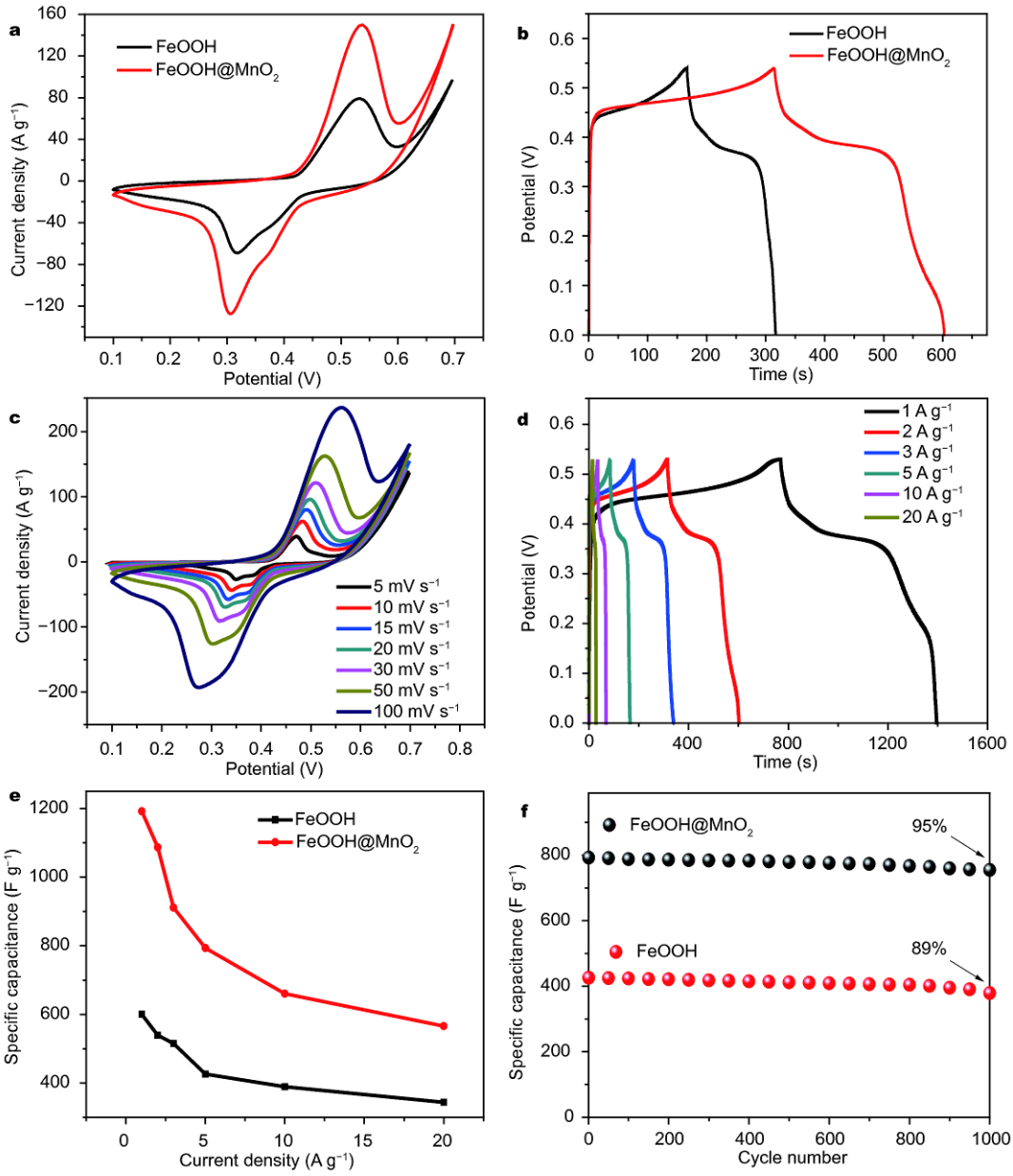

Figure 4 (a) Comparison of CV curves of the FeOOH and FeOOH@MnO_2 electrodes at scan rate of 50 mV s^{-1}; (b) comparison of GCD curves of the FeOOH and FeOOH@MnO_2 electrodes at current density of 2 A g^{-1}; (c) CV curves of FeOOH@MnO_2 at various scan rates; (d) GCD curves of FeOOH@MnO_2 electrode at different current densities of 1, 2, 3, 5, 10, and 20 A g^{-1}, respectively; (e) variation in specific capacitance with current density, and (f) cycling performance of the FeOOH and FeOOH@MnO_2 electrodes for 1000 cycles at 5 A g^{-1}.

of the electrode and electrolyte has been enhanced with 3D hierarchical hollow structure; (3) in this special architecture, FeOOH nanofibers as the "core" create channels for the effective mass transport of electrolyte, and the ultrathin MnO_2 as the "shell" can provide a short ion diffusion path to enable the fast and reversible faradic reaction.

CONCLUSIONS

In summary, hierarchical urchin-like FeOOH@MnO_2 hollow spheres have been designed and synthesized by a facile hydrothermal route. The as-fabricated FeOOH@MnO_2 shows enhanced electrochemical performance with a high specific capacitance (1192 F g^{-1} at 1 A g^{-1}), superior rate capability and excellent cycling

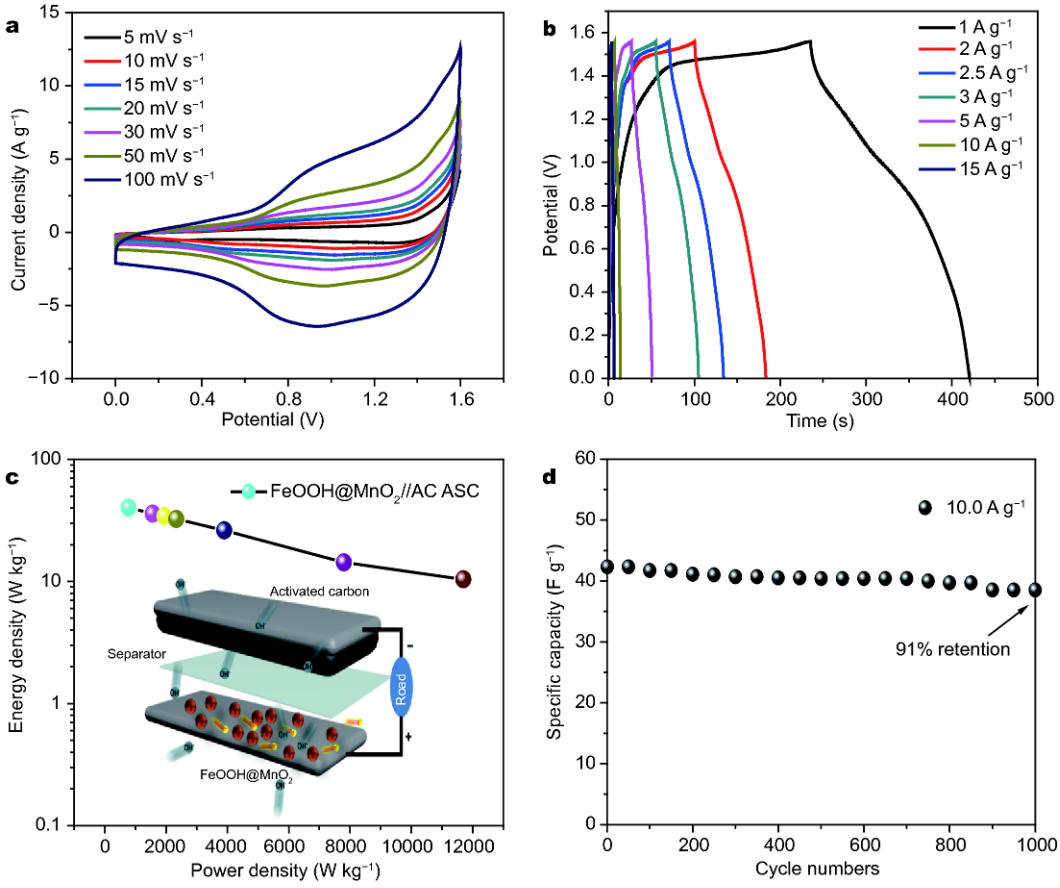

Figure 5 (a) CV curves of the FeOOH@MnO_2//AC ASC at various scan rates; (b) GCD curves of FeOOH@MnO_2 at various current densities; (c) the Ragone of the energy densities and power densities of FeOOH@MnO_2 and the inset is schematic showing ASC device construction using FeOOH@MnO_2 and AC electrodes; (d) cycling performance of FeOOH@MnO_2//AC ASC measured at a current density of 10 A g^{-1}.

stability, owing to the synergetic effect between the hierarchical FeOOH hollow microstructure and ultrathin MnO_2 nanolayer. An ASC device assembled from the FeOOH@MnO_2 and AC reaches a maximum energy density of 40.2 W h kg^{-1} at 0.78 kW kg^{-1} and 10.4 W h kg^{-1} at 11.7 kW kg^{-1}. Moreover, the capacitance retained 91% over 1000 cycles at current density of 10 A g^{-1}. The overall performance and cost effective synthesis of the FeOOH@MnO_2 make it a very promising material for alkaline electrolyte supercapacitors.

Received 14 June 2017; accepted 15 September 2017; published online 13 October 2017

1 Wang H, Dai H. Strongly coupled inorganic–nano-carbon hybrid materials for energy storage. Chem Soc Rev, 2013, 42: 3088–3113
2 Zhang GQ, Wu HB, Hoster HE, *et al.* Single-crystalline $NiCo_2O_4$ nanoneedle arrays grown on conductive substrates as binder-free electrodes for high-performance supercapacitors. Energ Environ Sci, 2012, 5: 9453–9456
3 Chu S, Majumdar A. Opportunities and challenges for a sustainable energy future. Nature, 2012, 488: 294–303
4 Miller JR, Simon P. Electrochemical capacitors for energy management. Science, 2008, 321: 651–652
5 Wang Z, Jia W, Jiang M, *et al.* One-step accurate synthesis of shell controllable $CoFe_2O_4$ hollow microspheres as high-performance electrode materials in supercapacitor. Nano Res, 2016, 9: 2026–2033
6 Zhang YQ, Li L, Shi SJ, *et al.* Synthesis of porous Co_3O_4 nanoflake array and its temperature behavior as pseudo-capacitor electrode. J Power Sources, 2014, 256: 200–205
7 Wu ZS, Zhou G, Yin LC, *et al.* Graphene/metal oxide composite electrode materials for energy storage. Nano Energ, 2012, 1: 107–131
8 Liu M, Gan L, Xiong W, *et al.* Development of MnO_2/porous carbon microspheres with a partially graphitic structure for high performance supercapacitor electrodes. J Mater Chem A, 2014, 2: 2555–2562
9 Shang X, Chi JQ, Lu SS, *et al.* Carbon fiber cloth supported interwoven WS_2 nanosplates with highly enhanced performances for supercapacitors. Appl Surf Sci, 2017, 392: 708–714
10 Li Y, Li Z, Shen PK. Simultaneous formation of ultrahigh surface area and three-dimensional hierarchical porous graphene-like networks for fast and highly stable supercapacitors. Adv Mater,

2013, 25: 2474–2480
11 Wu S, Zhu Y. Highly densified carbon electrode materials towards practical supercapacitor devices. Sci China Mater, 2017, 60: 25–38
12 Shinde SK, Dubal DP, Ghodake GS, *et al.* Nanoflower-like CuO/Cu$(OH)_2$ hybrid thin films: synthesis and electrochemical supercapacitive properties. J Electroanal Chem, 2014, 732: 80–85
13 Wei G, Du K, Zhao X, *et al.* Carbon quantum dot-induced self-assembly of ultrathin $Ni(OH)_2$ nanosheets: a facile method for fabricating three-dimensional porous hierarchical composite micro-nanostructures with excellent supercapacitor performance. Nano Res, 2017, 10: 3005–3017
14 Wang JG, Yang Y, Huang ZH, *et al.* Interfacial synthesis of mesoporous MnO_2/polyaniline hollow spheres and their application in electrochemical capacitors. J Power Sources, 2012, 204: 236–243
15 Xu J, Wang Q, Wang X, *et al.* Flexible asymmetric supercapacitors based upon Co_9S_8 nanorod//Co_3O_4@RuO_2 nanosheet arrays on carbon cloth. ACS Nano, 2013, 7: 5453–5462
16 Inagaki M, Konno H, Tanaike O. Carbon materials for electrochemical capacitors. J Power Sources, 2010, 195: 7880–7903
17 Yuan C, Li J, Hou L, *et al.* Ultrathin mesoporous $NiCo_2O_4$ nanosheets supported on Ni Foam as advanced electrodes for supercapacitors. Adv Funct Mater, 2012, 22: 4592–4597
18 Zhou C, Zhang Y, Li Y, *et al.* Construction of high-capacitance 3D CoO@polypyrrole nanowire array electrode for aqueous asymmetric supercapacitor. Nano Lett, 2013, 13: 2078–2085
19 Deori K, Ujjain SK, Sharma RK, *et al.* Morphology controlled synthesis of nanoporous Co_3O_4 nanostructures and their charge storage characteristics in supercapacitors. ACS Appl Mater Interfaces, 2013, 5: 10665–10672
20 Hu JS, Zhong LS, Song WG, *et al.* Synthesis of hierarchically structured metal oxides and their application in heavy metal ion removal. Adv Mater, 2008, 20: 2977–2982
21 Cao M, Liu T, Gao S, *et al.* Single-crystal dendritic micro-pines of magnetic α-Fe_2O_3: large-scale synthesis, formation mechanism, and properties. Angew Chem Int Ed, 2005, 44: 4197–4201
22 Zhang T, Zhang X, Ng J, *et al.* Fabrication of magnetic cryptomelane-type manganese oxide nanowires for water treatment. Chem Commun, 2011, 47: 1890–1892
23 Zeng Y, Yu M, Meng Y, *et al.* Iron-based supercapacitor electrodes: advances and challenges. Adv Energ Mater, 2016, 6: 1601053
24 Choi WS, Koo HY, Zhongbin Z, *et al.* Templated synthesis of porous capsules with a controllable surface morphology and their application as gas sensors. Adv Funct Mater, 2007, 17: 1743–1749
25 Nie Z, Wang Y, Zhang Y, *et al.* Multi-shelled α-Fe_2O_3 microspheres for high-rate supercapacitors. Sci China Mater, 2016, 59: 247–253
26 Huang M, Li F, Dong F, *et al.* MnO_2-based nanostructures for high-performance supercapacitors. J Mater Chem A, 2015, 3: 21380–21423
27 Reddy AE, Anitha T, Gopi CVVM, *et al.* Fabrication of a snail shell-like structured MnO_2@$CoNiO_2$ composite electrode for high performance supercapacitors. RSC Adv, 2017, 7: 12301–12308
28 Cheng G, Xie S, Lan B, *et al.* Phase controllable synthesis of three-dimensional star-like MnO_2 hierarchical architectures as highly efficient and stable oxygen reduction electrocatalysts. J Mater Chem A, 2016, 4: 16462–16468
29 Zhu J, Tang S, Xie H, *et al.* Hierarchically porous MnO_2 microspheres doped with homogeneously distributed Fe_3O_4 nanoparticles for supercapacitors. ACS Appl Mater Interfaces, 2014, 6: 17637–17646
30 He Y, Chen W, Li X, *et al.* Freestanding three-dimensional graphene/MnO_2 composite networks as ultralight and flexible supercapacitor electrodes. ACS Nano, 2013, 7: 174–182
31 Yang P, Ding Y, Lin Z, *et al.* Low-cost high-performance solid-state asymmetric supercapacitors based on MnO_2 nanowires and Fe_2O_3 nanotubes. Nano Lett, 2014, 14: 731–736
32 Wang H, Xu Z, Yi H, *et al.* One-step preparation of single-crystalline Fe_2O_3 particles/graphene composite hydrogels as high performance anode materials for supercapacitors. Nano Energ, 2014, 7: 86–96
33 Lu X, Zeng Y, Yu M, *et al.* Oxygen-deficient hematite nanorods as high-performance and novel negative electrodes for flexible asymmetric supercapacitors. Adv Mater, 2014, 26: 3148–3155
34 Yang S, Song X, Zhang P, *et al.* Self-assembled α-Fe_2O_3 mesocrystals/graphene nanohybrid for enhanced electrochemical capacitors. Small, 2014, 10: 2270–2279
35 Lu XF, Wu DJ, Li RZ, *et al.* Hierarchical $NiCo_2O_4$ nanosheets@hollow microrod arrays for high-performance asymmetric supercapacitors. J Mater Chem A, 2014, 2: 4706–4713
36 Chen YC, Lin YG, Hsu YK, *et al.* Novel iron oxyhydroxide lepidocrocite nanosheet as ultrahigh power density anode material for asymmetric supercapacitors. Small, 2014, 10: 3803–3810
37 Chemelewski WD, Lee HC, Lin JF, *et al.* Amorphous FeOOH oxygen evolution reaction catalyst for photoelectrochemical water splitting. J Am Chem Soc, 2014, 136: 2843–2850
38 Yu Q, Meng X, Wang T, *et al.* Hematite films decorated with nanostructured ferric oxyhydroxide as photoanodes for efficient and stable photoelectrochemical water splitting. Adv Funct Mater, 2015, 25: 2686–2692
39 Barik R, Jena BK, Dash A, *et al. In situ* synthesis of flowery-shaped α-FeOOH/Fe_2O_3 nanoparticles and their phase dependent supercapacitive behaviour. RSC Adv, 2014, 4: 18827–18834
40 Rao CNR, Sarma DD, Vasudevan S, *et al.* Study of transition metal oxides by photoelectron spectroscopy. Proc R Soc A-Math Phys Eng Sci, 1979, 367: 239–252
41 Wang Q, Liu B, Wang X, *et al.* Morphology evolution of urchin-like $NiCo_2O_4$ nanostructures and their applications as psuedocapacitors and photoelectrochemical cells. J Mater Chem, 2012, 22: 21647–21653
42 Zhu Y, Wu Z, Jing M, *et al.* Porous $NiCo_2O_4$ spheres tuned through carbon quantum dots utilised as advanced materials for an asymmetric supercapacitor. J Mater Chem A, 2015, 3: 866–877
43 Zhou H, Liu L, Wang X, *et al.* Multimodal porous CNT@TiO_2 nanocables with superior performance in lithium-ion batteries. J Mater Chem A, 2013, 1: 8525–8528
44 Wang M, Li Z, Wang C, *et al.* Novel core-shell FeOF/$Ni(OH)_2$ hierarchical nanostructure for all-solid-state flexible supercapacitors with enhanced performance. Adv Funct Mater, 2017, 27: 1701014
45 Chen J, Xu J, Zhou S, *et al.* Amorphous nanostructured FeOOH and Co–Ni double hydroxides for high-performance aqueous asymmetric supercapacitors. Nano Energ, 2016, 21: 145–153
46 Wei W, Cui X, Chen W, *et al.* Manganese oxide-based materials as electrochemical supercapacitor electrodes. Chem Soc Rev, 2011, 40: 1697–1721
47 Liu J, Jiang J, Bosman M, *et al.* Three-dimensional tubular arrays of MnO_2–NiO nanoflakes with high areal pseudocapacitance. J Mater Chem, 2012, 22: 2419–2426

Acknowledgements This work was supported by the National Natural Science Foundation of China (21771137), Shandong Provincial Natural

Science Foundation (ZR2016BM12), the Fundamental Research Funds for the Central Universities (15CX08010A), and the starting-up fund from TJUT.

Author contributions Du K designed and engineered the samples; Du K wrote the draft with discussion of Wei G, Zhao F, Li J, and An C. Wang H performed the SEM and XRD characterization. An CH supervised the projects and carefully reviewed and revised this manuscript. All authors contributed to the general discussion.

Conflict of interest The authors declare that they have no conflict of interest.

Supplementary information Supporting data are available in the online version of the paper.

Kun Du is currently a Master student in materials science from China University of Petroleum. Her research interests include the synthesis, characterization, and explorations of efficient catalysts in the fields of clean energy production and environmental purification.

Changhua An received his PhD degree from the University of Science and Technology of China (USTC) in 2003. In 2013, he was promoted to full professor of materials science. Now he is a professor at Tianjin University of Technology. His research interests focus on the synthesis, characterization, and explorations of efficient catalysts in the fields of clean energy production and environmental purification.

超薄MnO_2层修饰的海胆状空心FeOOH微米球及其在提高电容性能中的应用

杜坤[1,2], 魏桂涓[1,2], 赵福振[1,2], 安超[2], 王辉[1], 李金全[1,2], 安长华[1,2*]

摘要 本文通过简便的水热技术合成了超薄MnO_2修饰的海胆状FeOOH空心微纳米球. 该微米球由直径10 nm的纳米纤维组成. 由于FeOOH独特的微纳米结构和MnO_2的协同效应, 所制备的FeOOH@MnO_2电极在电流密度1 A g^{-1}下表现出1192 F g^{-1}的比电容, 同时显示出较高的倍率性能和优异的稳定性. 而且由FeOOH@MnO_2电极和活性炭组装的非对称电容器在0.78 kW kg^{-1}的功率密度下具有40.2 W h kg^{-1}的能量密度; 在较高的11.7 kW kg^{-1}功率密度下, 功率密度仍能保持在10.4 W h kg^{-1}.

